Impact of Ceramic Matrix Composite Topology on Overall Effectiveness

Ryan D. Edelson[1]
Department of Mechanical Engineering,
The Pennsylvania State University,
University Park, PA 16801
e-mail: rde13@pitt.edu

Karen A. Thole
Department of Mechanical Engineering,
The Pennsylvania State University,
University Park, PA 16801
e-mail: kthole@psu.edu

Ceramic matrix composites (CMCs) are a material of interest for components in the hot section of gas turbine engines due to their high strength-to-weight ratio and high temperature capabilities. CMCs are a class of material made of macro scale woven ceramic fibers infiltrated with a ceramic matrix making them significantly different than their nickel superalloy counterparts. As CMCs are implemented into gas turbine engines, the effects of the inherent topology of the CMC weave on convective heat transfer must be understood. In this study, film cooling holes were integrated into a representative CMC weave for three test coupons that were printed using additive manufacturing. The three coupons included: one having a weave topology along the surface of the internal channel supplying coolant to the film cooling holes; one having a weave topology along the external film cooled surface; and one having a weave topology on both the coolant supply channel as well as the external film cooled surface. Overall effectiveness levels for the two cases with a weave surface on the external film cooled wall were measured to be lower than levels for the case with the smooth external surface. The external weave significantly increased the mixing of the coolant jet with the hot mainstream resulting in poor cooling. [DOI: 10.1115/1.4055749]

Keyword: heat transfer and film cooling

Introduction

Ceramic matrix composites (CMCs) can lead to increased gas turbine efficiencies through increased operating temperatures and reduced cooling flows. CMCs have a structure made of woven ceramic fibers distributed within a ceramic matrix. The CMC structure increases the fracture toughness over traditional monolithic ceramics, while maintaining the favorable thermal properties of ceramic materials. High strength-to-weight ratio at high temperatures makes CMCs a desirable material choice over the nickel super alloys often used in hot section components of today's gas turbine engines [1,2]. This class of ceramics has the ability to increase turbine inlet temperatures and is suitable for a wide range of components throughout the engine [3]. Watanabe et al. [4,5] tested full-scale vanes and blades in thermal shock tests as well as over 400 h in actual engine environments, showing that CMC components had thermal lifespan capabilities that were relevant to engine operation.

With CMCs as a potentially advantageous material to utilize in gas turbine engines, it is of interest to fully understand the performance of these materials. A substantial difference between CMCs and their nickel superalloy counterparts is the surface topology resulting from the macro scale weave surface of CMCs. This weave surface has potential impacts on aero and heat transfer performance for components throughout the engine.

One of the keys to utilizing CMCs specifically within components in the hot section of a gas turbine engine will be to determine the impact of how a weave surface affects cooling performance metrics for turbine vanes and blades. Specifically, understanding how the weave surface impacts film cooling and how to integrate film cooling schemes into CMC surfaces is necessary for fully realizing the potential of CMCs for gas turbine components. Characterizing film cooling performance for CMC components is necessary to determine operational part temperatures and cooling flow

requirements. This study uniquely evaluates how a weave surface topology affects overall effectiveness.

Literature Review

CMCs offer several unique properties that are of interest to engine manufacturers for use in components in the hot section of gas turbine engines. To date, the focus of open literature on CMCs has been on their mechanical and thermal performance properties. In depth analysis of rupture strength, fatigue creep, thermal residual stress, ballistic impact performance, and other complex failure phenomena have been characterized for a multitude of CMC weave architectures [6–8].

There is still need for further characterization of CMCs, particularly in how the macro scale weave surface topology, inherent to CMCs and not present in superalloy components, will impact cooling performance parameters. A few researchers have looked at how a weave topology, representative of CMCs, impacts convective heat transfer performance. Krishna and Ricklick [9] conducted experiments observing the effects of a CMC weave on jet impingement. The surface was machined to maximize accuracy and minimize surface roughness. The researchers observed that the weave surface had negligible effects on heat transfer for jet impingement when compared to a smooth surface.

In a more recent study by Wilkins et al. [10], the impact of a weave topology on heat transfer and boundary layer development for an external flow was evaluated. The particular weave topology they used was a five-harness satin (5HS) weave, defined by Nemeth et al. [11] who determined the 5HS weave to be relevant for this application. Wilkins et al. [10] oriented the weave both parallel and perpendicular to the flow direction. This particular weave pattern was the same as that chosen for our study presented in this paper. Wilkins et al. [10] measured local variations in Stanton number between 20% and 40% higher than a smooth flat plate Stanton number as a result of the peaks and valleys of the weave topology. However, area averaged Stanton numbers were within experimental uncertainty of those measured for a smooth plate.
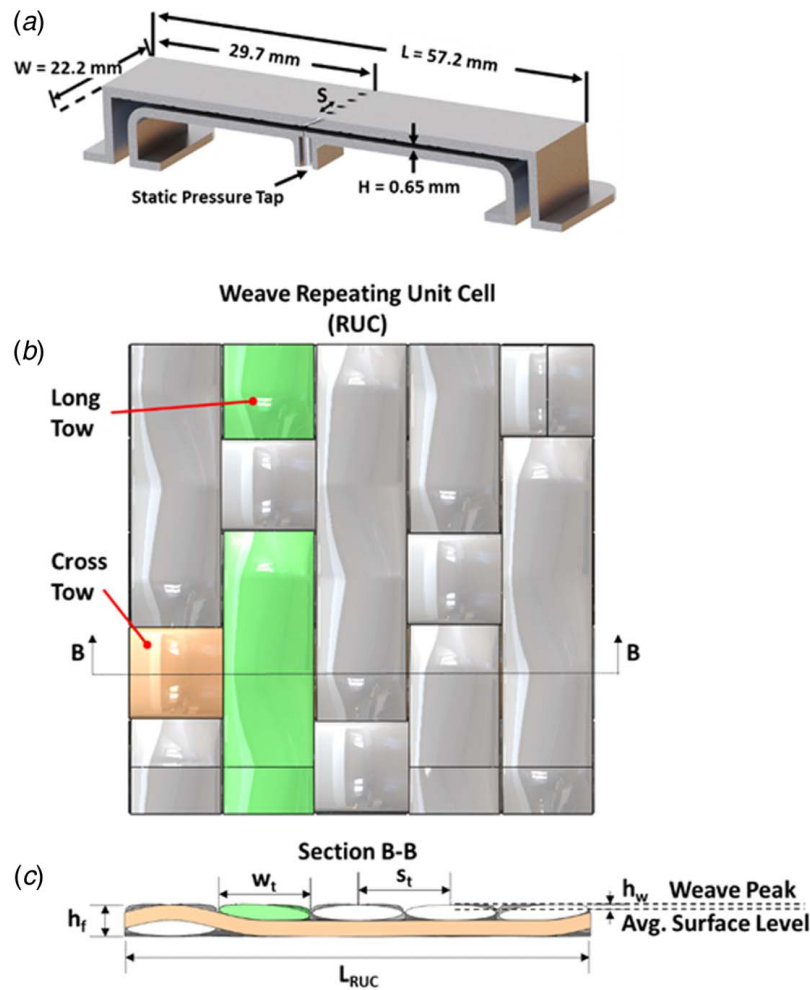
Fig. 1 (a) The overall coupon features and dimensions. ((b) and (c)) A top-down view and a cross-sectional view of the five-harness satin weave RUC from Ref. [13].

In a follow up study, Wilkins et al. [12] expanded their work by conducting conjugate computational fluid dynamics (CFD) simulations evaluating adiabatic effectiveness levels for film cooling over the same 5HS weave. They found that when the long weave strands were aligned with the film injection, the laterally averaged effectiveness levels were reduced below that of when the jet was injected along a smooth wall. However, by rotating the weave surface 90 deg, laterally averaged effectiveness values were improved beyond that of a smooth flat plate. Their predictions indicated periodic variation in the laterally averaged effectiveness due to the periodicity of the weave surface topology.

Cory et al. [13] investigated the directional effects of a weave topology by also using the 5HS weave on internal channel flows. In considering only one channel wall, they positioned the weave pattern with the long weave strands parallel and perpendicular to the flow, which augmented the averaged heat transfer by 25% and 40%, respectively, relative to a smooth channel. These augmentation levels were significantly higher than those reported by Wilkins et al. [12] in their large-scale external flow experiments. Additionally, when two channel walls included the weave surface, offsetting weave patterns from one another reduced friction factor augmentation by 10% without decreasing the heat transfer augmentation when compared to mirroring the weave pattern on opposing walls.

There is a gap in understanding how a representative CMC weave pattern affects film cooling performance as cooling holes are integrated into CMC components. Our study addresses this gap by

evaluating the following three engine scale coupons in conjugate heat transfer experiments with film cooling: (i) weave surface on one wall of the internal coolant supply channel with smooth external film cooled surface; (ii) weave surface on the external film cooled surface with smooth coolant supply channel walls; and (iii) a combined weave surface on both the internal coolant supply channel and external film cooled surface. This study was unique because it methodically evaluated each of these contributions to component cooling and seeks to fill a gap in the knowledge required for integrating film cooling into hot section components made using CMC.

Weave Pattern and Test Coupon Geometry

Film cooled test coupons were designed at a true scale (1×) relevant to hot section gas turbine hardware. Figure 1(a) shows a description of the test coupons describing both the overall coupon dimensions as well as the dimensions of the single internal channel. Each coupon had an internal channel that provided coolant to the cooling holes in a co-flow configuration relative to the mainstream.

Each of the test coupons had the weave pattern oriented such that the long tows were parallel with the mainstream flow direction. Figure 1(b) shows a top-down view of the weave repeating unit cell (RUC), which was the same weave RUC used by Cory et al. [13] and Wilkins et al. [10,12]. This unit cell was repeated across

the relevant coupon surfaces to create the weave pattern. This weave pattern was generated using a program that allows users to define custom weave patterns called TexGen [14]. Figure 1(c) shows a cross section of the same RUC from Cory et al. [13]. The 5HS weave RUC had a total of five long tows, with each long tow being overlapped by a cross tow exactly once per RUC. The tow and RUC dimensions were scaled to match those described in Ref. [11]. Table 1 lists the weave RUC dimensions in terms of the width (W) of the external surface, as well as both the height of the internal channel of $H_i = 0.65$ mm. The height of the external mainstream channel was $H_e = 9.5$ mm which was equal to 25 cooling hole diameters. The weave RUC dimensions remained constant for both internal and external surfaces, but the weave peaks extend farther into the flow for the internal channel due to its decreased channel height when compared to the mainstream channel.

At the streamwise mid-location was a row of nine film cooling holes, defined by the geometric parameters seen in Table 2. The cooling hole shape used in all coupons for this study was the baseline 7-7-7 shaped hole, which is a laidback fan shaped cooling hole described by Schroeder and Thole [15]. The metered hole diameter was $D = 0.38$ mm, relevant to real engine scales. The overall coupon dimensions, internal channel dimensions, and hole dimensions and geometries were kept constant for all coupons.

The laser powder bed fusion method for additive manufacturing (AM) was utilized to construct the test coupons with the previously mentioned 5HS weave geometry. All coupons were AM printed from Inconel 718, which has a known as-manufactured thermal conductivity. During the printing process, the coupons were angled at a 60 deg angle relative to the build plate, such that the film cooling holes were printed vertically.

Three total test coupons of varying geometry were printed, as seen in Figs. 2(a)–2(c). These coupons were: the internal CMC coupon, Fig. 2(a), that had a weave surface on the top wall of the coolant supply channel, with a smooth external film cooled surface; the external CMC coupon, Fig. 2(b), that had a smooth coolant supply channel, with an external film cooled weave surface; and the internal + external CMC coupon, Fig. 2(c), that had weave surface on both the top wall of the coolant supply channel and external film cooled surface. All other walls of the internal channel had roughness levels inherent to the AM process.

The as-manufactured coolant channel and cooling hole dimensions were determined by analyzing computed tomography (CT) scans of each test coupon. Specialized software was used to calculate the perimeter and cross-sectional area of the internal coolant channel, as well as the cross-sectional area of the film cooling holes. The minimum cross-sectional area of each film cooling hole was summed to determine the blowing ratio (M). These minimum cross-sectional areas were within 5% of the average cross-sectional area for the metered section of the film cooling holes for a given test coupon. Similar to the work by Cory et al. [13], the hydraulic diameter for the internal channel with a weave surface was calculated using the CT scan data to determine an average (peak-to-trough) surface. These surface locations defined the rectangular cross section needed to calculate the hydraulic diameter.

Table 1 5HS weave dimensional parameters

Parameter	Size
RUC length, L_{RUC}	0.26 W
Tow width, w_t	0.05 W
Tow pitch, s_t	0.05 W
Internal fabric height, $h_{f,i}$	0.35 H_i
Internal weave peak, $h_{w,i}$	0.07 H_i
External fabric height, $h_{f,e}$	0.02 H_e
External weave peak, $h_{w,e}$	0.005 H_e

Table 2 7-7-7 shaped cooling hole dimensional parameters

Parameter	Value
Injection angle, α	30 deg
Laidback angle, β_{fwd}	7 deg
Lateral angle, β_{lat}	7 deg
Metered hole diameter	0.38 mm
P/D	6
H_i/D	1.7
H_e/D	25

In order to characterize the roughness of the weave surfaces compared to the inherent roughness from the additive manufacturing process, surface roughness measurements were taken of the external weave surface, before the test coupons were painted, which will be further explained in a later section. From these measurements, the arithmetic mean roughness (S_a) of the external weave surface was
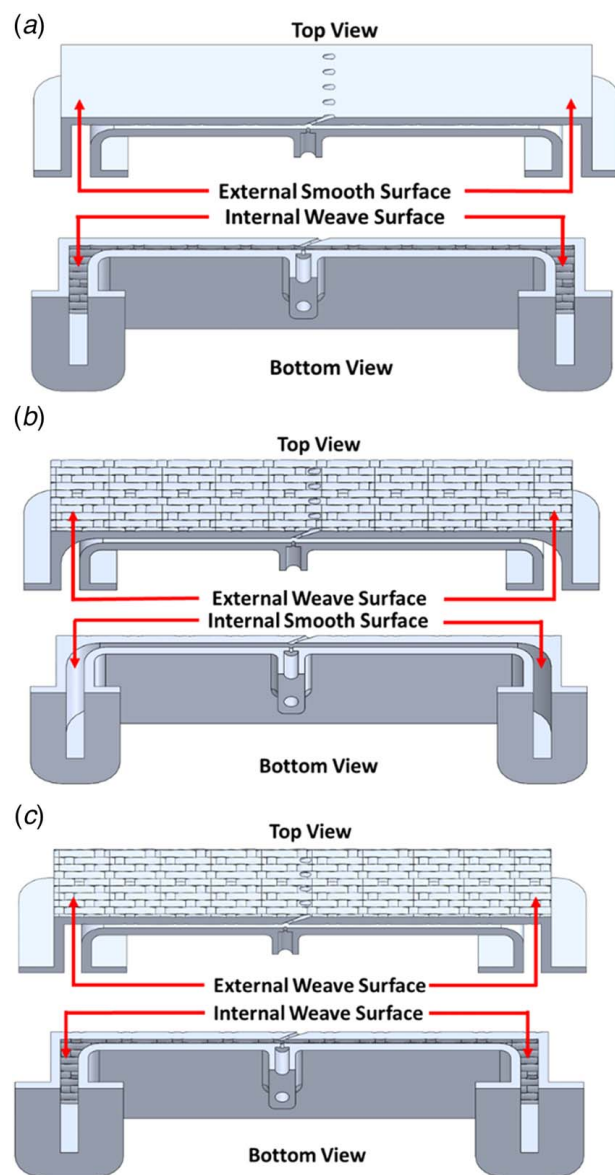

Fig. 2 Streamwise cross-sectional top and bottom views of weave film cooling coupons for (a) the internal CMC coupon, (b) the external CMC coupon, and (c) the internal + external CMC coupon

$S_a = 30 \ \mu m$. As a point of comparison, the arithmetic mean roughness inherent to the AM process, which is seen on all smooth walls in this study, is reported to be between $10 < S_a < 14 \ \mu m$, as characterized by Stimpson et al. [16] in work done with AM microchannels.

Experimental Setup and Methodology

Overall effectiveness measurements were made using a test rig that was the same as the one used by Stimpson et al. [17,18]. Figure 3 shows a cross-sectional view of the test rig that consisted of a mainstream channel, a test coupon, and a plenum that both supplied the coolant and housed the instrumentation. Coolant was supplied to the row of film cooling holes through a co-flowing internal channel while the mainstream channel provided flow over the external surface. The mass flowrate through the film cooling holes was controlled by changing the pressure ratio (PR) across the cooling holes, which will be discussed in further detail later in this section.

Table 3 provides the operating parameters that were held constant during the overall effectiveness tests. A turbine flowmeter measured the flowrate of the mainstream channel, which supplied dry air at 60 °C, 345 kPa, and a constant Mach number of 0.3. The dimensions of the external mainstream channel were 25.4 mm wide and 9.5 mm tall (25 cooling hole diameters). Upstream, the channel had sufficient length such that the flow that passes over the external surface of the test coupon was hydrodynamically developed.

To achieve the desired density ratio for these experiments of DR = 1.2, gaseous nitrogen (N_2) was used as the coolant gas. The flowrate of the coolant supply was measured using a laminar flow element downstream of the test section to ensure that the downstream internal Reynolds number (Re_{Dh}) of the coolant supply

channel was matched for each test. The flowrate through the film cooling holes was determined using a relation developed through experiments as a function of the pressure ratio across the film cooling holes. Pressure taps were installed in the mainstream channel, as well as within each coupon at the film cooling hole location, to ensure accurate pressure ratio measurements. Nondimensionalizing the mass flow into a flow parameter (FP) allowed for the mass flowrate through the film cooling holes to be known for a particular pressure ratio. For every blowing ratio, the coolant supply channel downstream of the film cooling holes was kept constant at $Re_{Dh} = 14{,}000$, while the upstream Re_{Dh} varied between blowing ratios given the film cooling flow was extracted as indicated in Table 3. The intention of holding the downstream Re_{Dh} constant was to ensure the same downstream boundary condition for all film cooling tests. In defining the blowing ratio, the centerline velocity (U_∞) was used as the scaling velocity for the external flow over the test coupon. A one-seventh power velocity profile was assumed, resulting in an external velocity of $U_\infty = 1.224V_\infty$, where V is the mass averaged velocity through the mainstream channel [19].

The internal heat transfer coefficient (h_i) and external heat transfer coefficient (h_∞) were both experimentally determined for the AM external surface and internal coolant supply channel, both with no weave topology. From these measurements, the Biot number for this study was Bi = 0.3 and the convective heat transfer ratio was h_∞/h_i = 1, 2. It was of interest for the authors to maintain values of both Bi and convective heat transfer ratios within a range relevant for turbine components. As a point of reference, Stimpson et al. [17] report values of Bi = 0.1 and h_∞/h_i = 1 as being relevant to turbines.

As shown in Fig. 3, a zinc selenide window with a constant transmissivity of 0.7 was placed above the coupon to provide optical access for the infrared (IR) thermography measurements. The test coupons and test rig were painted black to maximize surface emissivity, which was assumed to be a constant 0.95. To calibrate the IR camera, a calibration test was conducted prior to each set of coupon tests, where the coupon surface was varied between −10 °C and 30 °C. Thermocouples at two different locations were placed on the external surface of each test coupon and were used to calibrate the infrared images. A linear calibration curve was used to calculate the surface temperatures.

The goal of this study was to investigate how overall effectiveness, ϕ, was affected by the different combinations of weave geometries seen in Figs. 2(a)–2(c) both with and without film cooling. Because there was heat transferred to the coolant upstream of the film cooling injection, the coolant temperature at the film cooling injection location had to be determined for use in the overall effectiveness calculation. The heat transfer to the coolant was quantified by conducting an additional test for each coupon geometry with blocked cooling holes. The cooling holes were blocked by sealing the exit of the holes with a thin layer of kapton adhesive. For the blocked cooling holes, it was assumed that the surface temperature between the bottom, side, and top walls was constant through the length of the channel. This provided a constant surface temperature boundary condition along the internal coolant supply channel upstream of the cooling holes. With the external surface temperature measured by the IR camera, and the inlet and exit coolant temperatures measured, a 1D conduction analysis was done to determine the internal heat transfer coefficients, h_i. To validate the calculations, these deduced values of h_i were used to estimate the coolant exit temperature for the overall effectiveness tests, accounting for the loss in mass flow in the coolant supply channel for the film cooling cases. The comparisons indicated the estimates were within 2 °C at the highest M, and within 1 °C at lower M. These h_i values were then used to calculate the coolant temperature in the channel at the entrance to the cooling hole.

Fig. 3 Schematic of the experimental rig used for overall effectiveness experiments

Table 3 Film cooling test rig flow parameters

Parameter	Internal flow	External flow
Mach number	0.1	0.3
Upstream Re_{Dh}	15,000–21,000	N/A
Downstream Re_{Dh}	14,000	N/A
Re_L	N/A	900,000
Film cooling DR	1.2	
Bi	0.3	
h_∞/h_i	1.2	

Experimental Uncertainty. Overall uncertainty was calculated for the three key parameters for this study: ϕ, Re, and M, using the method described by Figliola and Beasley [20]. The uncertainty in
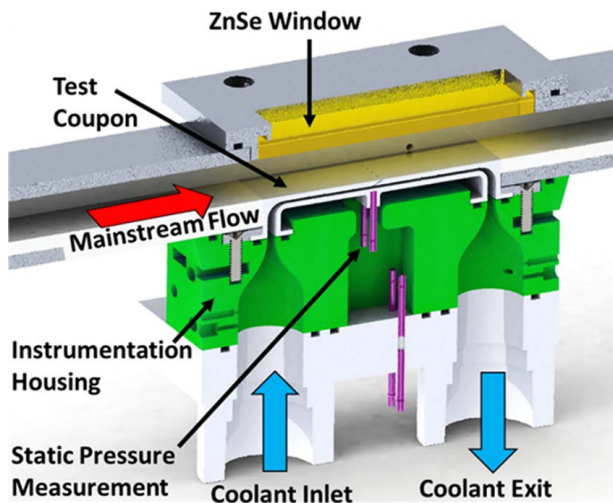
Re for both the internal coolant channel and mainstream channel was under 5%. The uncertainty in M was 10%, which was largely due to the uncertainty in the hole metering area based on the CT scan measurements. The uncertainty in ϕ was ±0.06 for a blowing ratio of $M = 0.6$ and ±0.07 for a blowing ratio of $M = 3.0$. This uncertainty was mostly driven by the uncertainty in the temperature measurements taken by the IR camera and the calculated coolant temperature.

In addition to the measurement uncertainty, repeatability measurements were carried out, where the test rig was taken apart and put together again. Repeatability tests were run twice, for multiple coupons in this study. The results from this found that there was a repeatability uncertainty of $\phi = \pm0.03$.

Overall Effectiveness Benchmarking

A benchmarking experiment was conducted by testing an additively manufactured film cooling coupon from Stimpson et al. [17], specifically the 1x-A-2H-EDM coupon which was referred to by their paper. While the benchmark coupon dimensions and film cooling holes were very similar to those that were used for the weave topology coupons, there were two important differences. First, the internal channel height, H_i, for the benchmark coupon was 1.3 mm, rather than 0.65 mm for the weave topology coupons. Additionally, while the film cooling hole shape, size, and spacing of the benchmark coupon matched the weave topology coupons, the film cooling holes for the benchmark coupon were manufactured through wire electrical discharge machining (EDM), rather than being directly printed into the coupon. The operating parameters of this benchmark test matched those used to test the weave topology coupons.

Figure 4 compares the resulting area averaged overall effectiveness results for the benchmark coupon between the current study and Stimpson et al.'s study [17]. Although there were consistently higher values of overall effectiveness reported by Stimpson et al. [17], the data were within 8% for the lowest blowing ratio, and within 3% for the highest blowing ratios, for which both were within the experimental uncertainty. As such, the data collected by Stimpson et al. [17] were matched, providing a successful benchmark for the test rig and data collection.

Overall Effectiveness for No Film Cooling

Each of the three weave topology coupons shown in Figs. 2(a)–2(c) were evaluated with blocked film cooling over a range of

Table 4 Overall effectiveness without film cooling values

Coupon	$\bar{\bar{\phi}}_0$
Internal CMC	0.55
External CMC	0.33
Internal + external CMC	0.36

internal coolant channel Reynolds numbers. These tests were conducted to provide a reference point for which to evaluate the film cooling benefit to the overall effectiveness. Table 4 reports the results of these tests for each of the three test coupons as the overall effectiveness without film cooling, ϕ_0. This ϕ_0 test was conducted at a channel Reynolds number of $\mathrm{Re}_{\mathrm{Dh}} = 14{,}000$.

Based on the results in Table 4, the two coupons that had the weave on the external surface (external CMC and internal + external CMC) resulted in significantly lower ϕ_0 when compared to the internal CMC coupon, which had a smooth external surface. These lower ϕ_0 values for the external CMC and internal + external CMC coupons indicate that the external weave surface increased the convective heat transfer between the warm mainstream flow and the test coupon when compared to a smooth surface, which reduced the overall effectiveness of the coupons.

Additionally, there was a slight increase in $\bar{\bar{\phi}}_0$ for the external + internal CMC coupon over the external CMC coupon. This trend shows that the increased heat transfer coefficient caused by the weave surface on the internal coolant supply channel increased overall effectiveness levels. From the magnitude of these differences, the external weave surface had a more significant impact than the internal weave surface on ϕ_0.

For the differences in the ϕ_0 values to occur as given in Table 4, the convective heat transfer augmentation above a smooth surface for the two coupons having the external weave surfaces (the external CMC and internal + external CMC coupons) was calculated to be on the order of 30%. These augmentation levels are consistent with those previously reported by Cory et al. [13] for their studies. However, Wilkins et al. [10] indicated that for external flow over the same weave topology as the current study, there was no increase in the convective heat transfer augmentation levels relative to that of a smooth surface. The current study and the study by Wilkins et al. [10] were both conducted at nearly the same external Reynolds number with our study being at a higher Mach number. One of the primary differences between our study and that of Wilkins et al. [10] is the particular scales between the two studies. Wilkins et al. [10] performed their measurements in a large-scale wind tunnel while our measurements were conducted at a scale that was 30× smaller than that of Wilkins et al. [10]. Resulting from this scale difference, we attribute the differences between the heat transfer augmentations to the effects of the channel side walls due to the inherent differences between the two experiments. For nearly the same scale as our study, where our current study was at 1× scale and the study by Cory et al. [13] was at 3× scale, the sidewall flow interactions have been
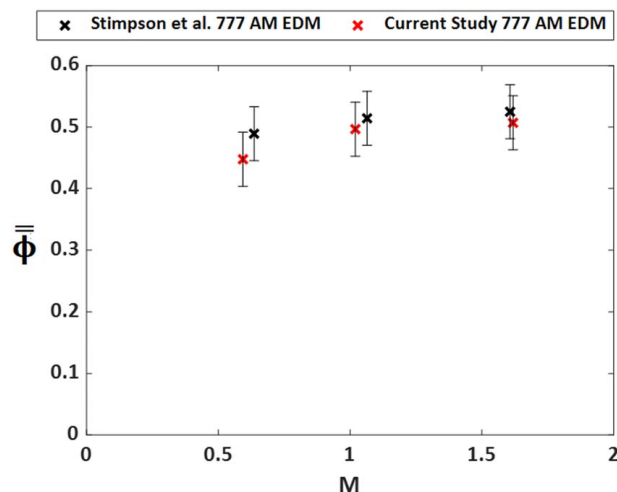

Fig. 4 Benchmark area averaged overall effectiveness values compared to those reported by Stimpson et al. [17] for an additively manufactured film cooling coupon with 7-7-7 shaped cooling holes manufactured through wire EDM
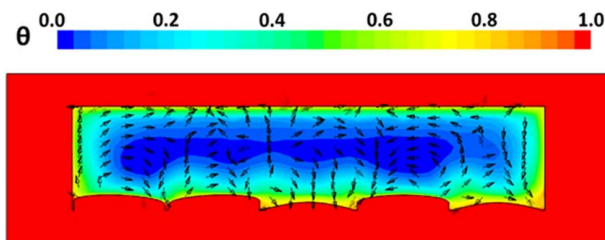

Fig. 5 CFD of an internal channel with a 5HS weave surface on one wall from Ref. [13]. Shown is a cross-sectional view of normalized temperature with secondary flow vectors.

previously reported by Cory et al. [13] through their computational simulations. As seen in Fig. 5 from Cory et al. [13], there were secondary flow structures that increased the mixing between the hot fluid near the weave wall and cold central core flow. These secondary flow structures are driven by interactions between the weave surface and sidewalls in the case of the small scale that would not have been a major factor in the large-scale wind tunnel studies. As such, increased secondary flow structures for the two coupons having the external weave surface in our study resulted in low effectiveness levels without film cooling.

Setting Film Cooling Flows

To characterize the mass flow through the film cooling holes, the measured flows were non-dimensionalized using the FP and blowing ratio (M) and evaluated over a range of PRs across the film cooling holes.

Figures 6(a) and 6(b) show flow parameter and blowing ratio for the range of pressure ratios used in the experiments. All film cooling holes were manufactured using the additive manufacturing process. The data in Fig. 6(a) indicate that the external CMC coupon had a significantly higher flow parameter for a given pressure ratio when compared to the other two coupon geometries. The reason for this difference was because the external CMC coupon had a smooth internal surface that supplied the coolant as compared with the other two coupons in which the weave surface disturbed the flow at the cooling hole entrance, the results in Fig. 6 imply that the weave surface caused distortions at the inlet of the hole resulting in higher pressure losses for the two coupons having the internal

Fig. 6 (a) FP versus PR for weave topology test coupons and (b) M versus PR for weave topology test coupons.

channel weave. These differences in the flow parameter were significant, considering at PR = 1.5, the internal + external CMC coupon saw a 26% reduction in FP when compared to the external CMC coupon. This reduction is also indicated by blowing ratio as shown in Fig. 6(b). Due to the decreased FP at a given PR, the internal and internal + external CMC coupons required a higher PR to achieve the same blowing ratio as the external CMC coupon. For example, to achieve a blowing ratio of $M = 1.5$, the internal + external CMC required a 12% increase in PR when compared to the external CMC coupon.

Previous work has shown that the geometry at the inlet of the film cooling holes has significant effects on cooling hole flowrates. For example, Hay et al. [21] measured discharge coefficient and showed that changes in inlet geometry can cause changes in discharge coefficient between 20% and 30%. Additionally, Hay et al. [21] showed that geometry distortions at the exit of the film cooling holes had almost no effect on discharge coefficient. These results from Ref. [21] support the trends seen by the data in our study, where distortion of the cooling hole inlet reduced FP, and distortion at the exit of the film cooling hole was much less significant, comparatively.

Overall Effectiveness With Film Cooling

Overall effectiveness, ϕ, was evaluated with film cooling for each test coupon from $0.6 < M < 3.0$ for the three film cooled coupons shown in Figs. 2(a)–2(c). To examine local variation in ϕ between test coupons, contour plots of ϕ can be seen in Fig. 7. For cases with an external weave surface, the weave surface geometry was superimposed onto the contour. Figure 7 extends 10 diameters spanwise in both directions from the center hole, and 20 diameters downstream from the set of film cooling holes. The contour plots shown are for $M = 0.6$, 1.5, and 3.0.

The data in Fig. 7 show ϕ levels increased as blowing ratio increased for all cases. Additionally, the highest regions of ϕ were surrounding the film cooling holes. These ϕ levels in the near hole regions indicated that in-hole convection was an important driver in increasing levels of ϕ for all three test coupons. This in-hole convective heat transfer increased with increasing blowing ratio as the mass flowrate of coolant through the film cooling holes increased.

The data in Fig. 7 also showed that for a given M, the external CMC had the lowest levels of ϕ, while the internal CMC had the highest levels of ϕ. This trend was caused by the different combinations of weave surface geometry, depending on if the weave surface was on the external film cooled surface or internal coolant supply channel. The weave surface on the internal coolant supply channel increased ϕ, when compared to a smooth surface, as the weave surface increased the heat transfer coefficient of the internal coolant channel. However, on the external side exposed to film cooling, the weave surface increased the mixing of the coolant with the mainstream flow when compared to a smooth surface. This increased mixing caused the coolant temperature to increase as it moved downstream of the film cooling holes. This increase in coolant temperature as it flowed downstream of the film cooling holes resulted in decreased ϕ levels for the coupons with an external weave surface compared to a smooth external surface. As such, the internal CMC coupon, which had a smooth external surface and weave surface on the top wall of the internal coolant feed channel, saw the highest ϕ.

To examine local ϕ values in a more quantitative manner, Figs. 8(a) and 8(b) show line plots of the contours seen in Fig. 7. Figure 8(a) provides centerline ϕ values, ϕ_{CL}, while Fig. 8(b) provides laterally averaged ϕ values, $\overline{\phi}$, where the lateral average was averaged over ±3 hole diameters in the spanwise direction over the three central film cooling holes for each coupon. All coupons were plotted at $M = 0.6$, 1.5, and 3.0. The location of $X/D = 0$ for Fig. 8 coincided with the exit of the film cooling hole as seen in Fig. 7. The effects of the film cooling jets are apparent in Figs. 8(a) and 8(b). At $X/D = 0$, the region at the exit of the hole, the highest levels of ϕ_{CL}
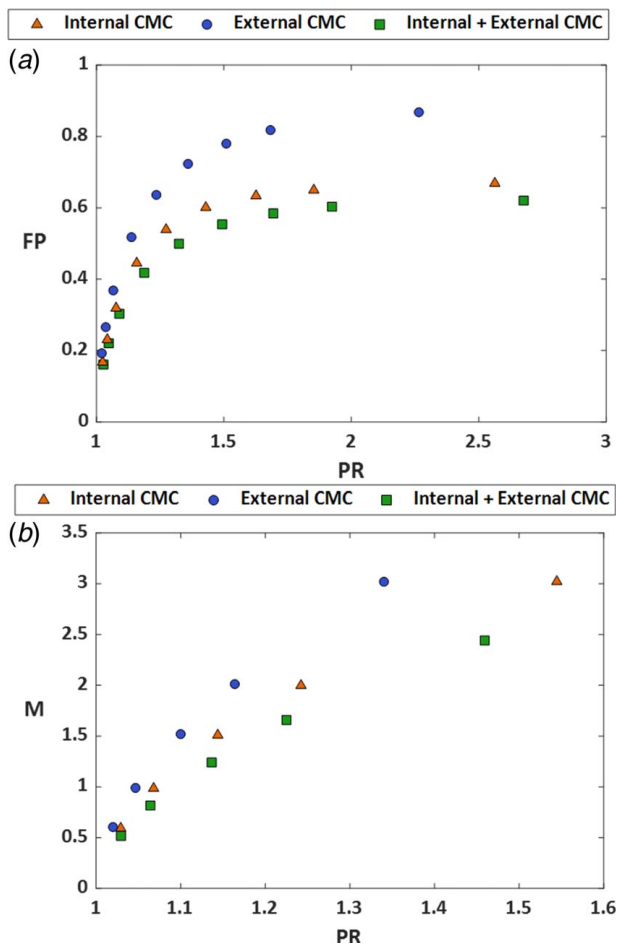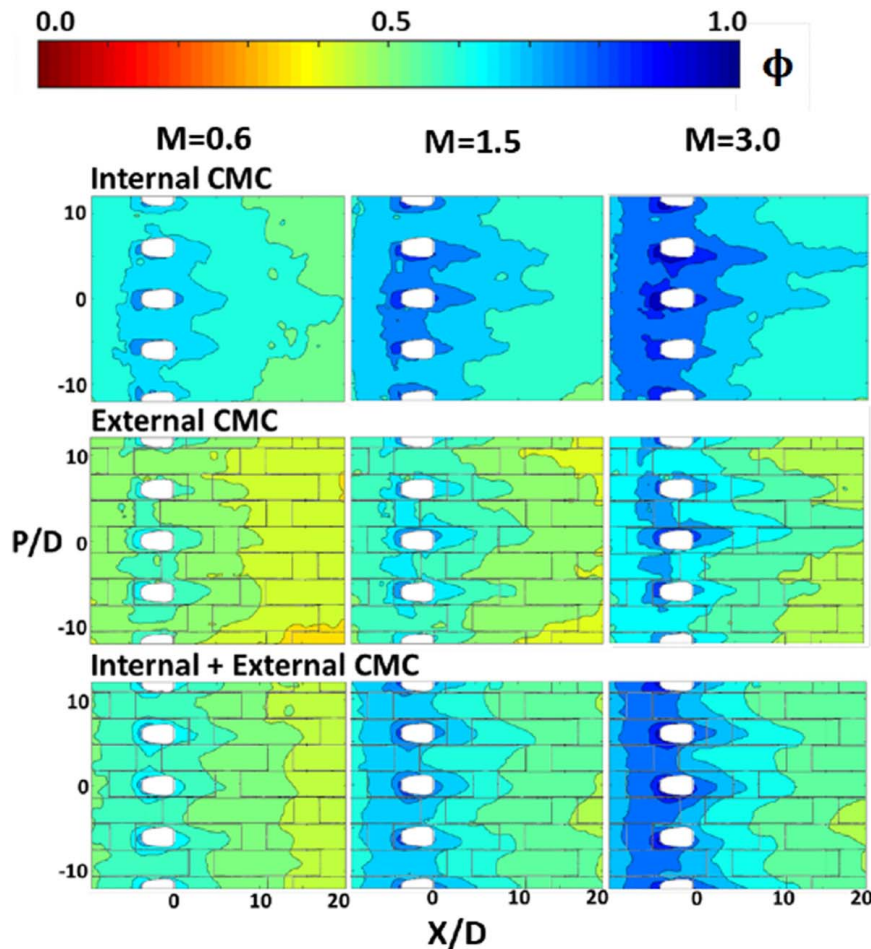
Fig. 7 Overall effectiveness contours for all three weave topology test coupons at $M = 0.6$, 1.5, and 3.0, with a view from 10 to −10 hole diameters in the spanwise direction, and 20 hole diameters downstream

and $\overline{\phi}$ were seen for all coupons at all blowing ratios, followed by decreased levels of ϕ_{CL} and $\overline{\phi}$. As X increased further downstream of the film cooling hole, the coolant temperature increased, and the film jet cooled the coupon surface less effectively.

The coupons with an external weave surface saw faster decays in ϕ_{CL} and $\overline{\phi}$ downstream of the film cooling holes because the external weave surface increased mixing, compared to a smooth external surface, between the coolant and mainstream flow as shown in Fig. 8. For example, from $\overline{\phi}$ values seen in Fig. 8(b), at $M = 3.0$ the internal + external CMC coupon had a decrease in $\overline{\phi}$ of 35% from $0 < X/D < 30$, while the internal CMC coupon, which had a smooth external surface, only had a decrease of 25% over the same streamwise distance.

For these tests with film cooling, it was of interest to characterize the effect that in-hole convection had on overall effectiveness. As such, Fig. 9 shows area averaged overall effectiveness for the regions upstream of and adjacent to the exit of the film cooling holes, ϕ_h. In Fig. 9, ϕ_h was averaged from $-6 < X/D < 0$, the beginning of this region coinciding with the entrance to the metered section of the film cooling holes, and $\pm 9D$ in the lateral direction. As can be seen in Fig. 9, increasing the blowing ratio caused an increase in ϕ_h for all coupons. This was due to the in-hole convective heat transfer, which increased with blowing ratio as the mass flowrate of coolant through the film cooling holes increased.

Additionally, Fig. 9 further highlights the effect of the internal coolant channel on ϕ_h. In the regions upstream of and adjacent to the film cooling holes, ϕ_h was only driven by the internal convective heat transfer from the coolant supply channel and the in-hole

convection from the film cooling holes. Figure 9 shows that the internal CMC and internal + external CMC coupon, which had a weave surface on the internal supply channel, saw an increase in ϕ_h compared to the external CMC coupon which had a smooth internal supply channel. The weave surface increased the heat transfer coefficient, compared to a smooth surface, of the internal coolant supply channel, which increased ϕ_h levels. For example, at $M = 1.5$, the internal CMC coupon saw a 12% increase in ϕ_h when compared to the external CMC coupon.

Figure 10 shows area averaged overall effectiveness, $\overline{\overline{\phi}}$, over a range of blowing ratios for all three weave topology coupons. This area average was taken $\pm 9D$ in the lateral direction, and from $0 < X/D < 30$. The $\overline{\overline{\phi}}$ trends were a consequence of the effects seen in Figs. 7–9. $\overline{\overline{\phi}}$ increased for all coupons with increasing blowing ratio. An external weave surface increased the mixing between the coolant and mainstream flows, decreasing $\overline{\overline{\phi}}$ levels. An internal weave surface increased the heat transfer coefficient of the internal coolant supply channel, increasing $\overline{\overline{\phi}}$ levels. As such, the internal CMC coupon showed the highest levels of $\overline{\overline{\phi}}$ for all blowing ratios as it had best combination of geometry features for driving increases in $\overline{\overline{\phi}}$.

Overall Effectiveness Augmentation

The benefit of film cooling to the levels of ϕ was evaluated for each test coupon. Isolating the benefit of film cooling was evaluated by defining the overall effectiveness augmentation, which is the
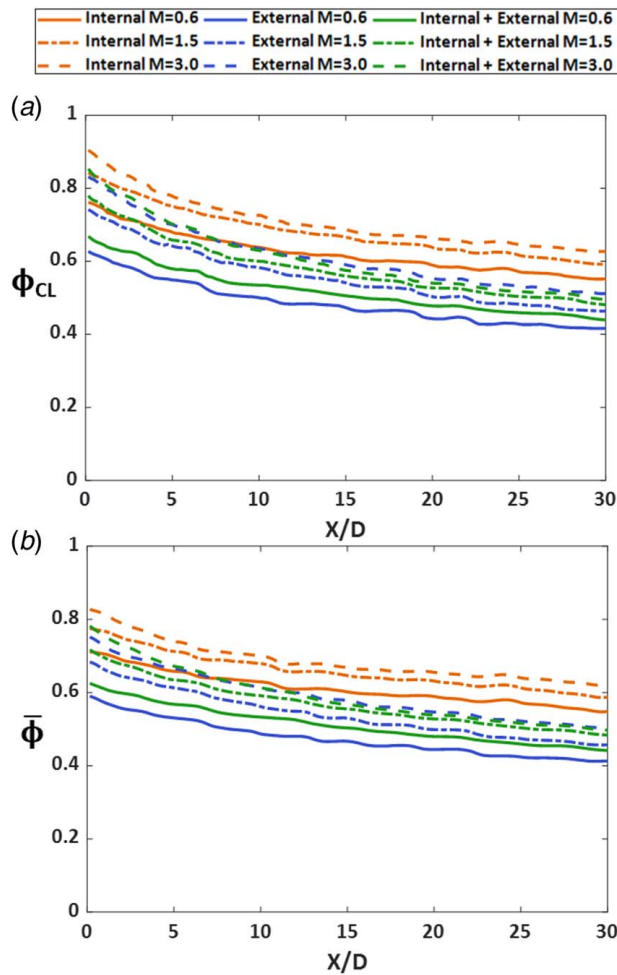
Fig. 8 (a) Centerline overall effectiveness and (b) laterally averaged overall effectiveness as a function of downstream distance, X/D, averaged over the three center film cooling holes

Fig. 9 Area averaged overall effectiveness in the upstream and near hole region. Averaged from $-6 < X/D < 0$ and $\pm 9D$ in the lateral direction.

Fig. 10 Area averaged overall effectiveness values for all three weave topology test coupons for a blowing ratio range of 0.6–3.0. Area average was taken $\pm 9D$ in the lateral direction, from $0 < X/D < 30$.

Fig. 11 Overall cooling effectiveness augmentation for a range of blowing ratios for all three weave topology test coupons

ratio of area averaged overall effectiveness with film cooling, $\bar{\bar{\phi}}$, to overall effectiveness without film cooling, $\bar{\bar{\phi}}_0$, from Fig. 10 and Table 4, respectively. The ratio between these two values was used to evaluate the benefit of adding film cooling jets to both an external weave and a smooth external surface. Figure 11 shows a plot of overall effectiveness augmentation for a range of blowing ratios for all three weave topology test coupons. As seen in Fig. 10, $\bar{\bar{\phi}}$ increased as a function of blowing ratio for all coupons. Since $\bar{\bar{\phi}}_0$ was a constant, the trend follows that overall effectiveness augmentation increased as a function of blowing ratio. From Fig. 11, each augmentation value was above one for all blowing ratios, which showed that film cooling was an effective method for reducing the temperature of the test coupon.

The test coupons with an external weave surface saw equal augmentation results, which were significantly greater than the augmentation seen by the test coupon with a smooth external surface. These results indicate that film cooling was more beneficial for reducing part temperatures for the coupons having an external weave surface when compared to a smooth external surface. One driver behind this trend was that the internal + external CMC and external CMC coupons had significantly decreased $\bar{\bar{\phi}}_0$ when compared to the internal CMC coupon. As previously discussed, this decrease in $\bar{\bar{\phi}}_0$ was because the external weave surface had an increased heat transfer coefficient when compared to a smooth surface, extracting more heat from the mainstream flow, which increased the coupon temperature and decreased $\bar{\bar{\phi}}_0$.

As was shown previously in Fig. 10, $\bar{\bar{\phi}}$ was decreased when an external weave surface was present relative to a smooth surface.
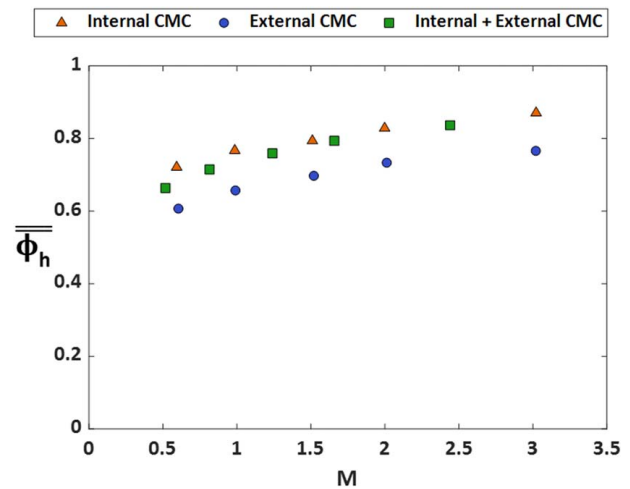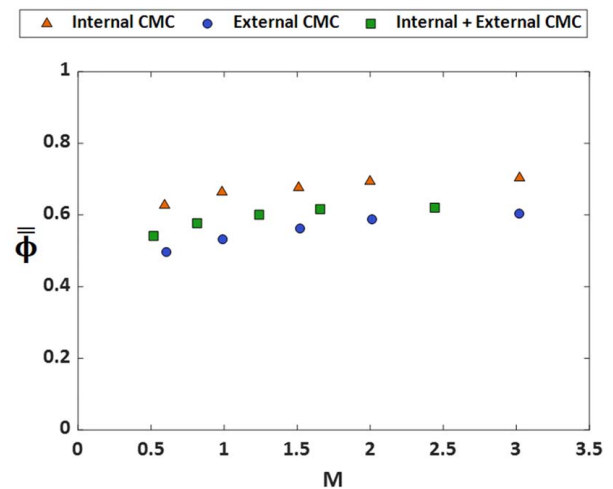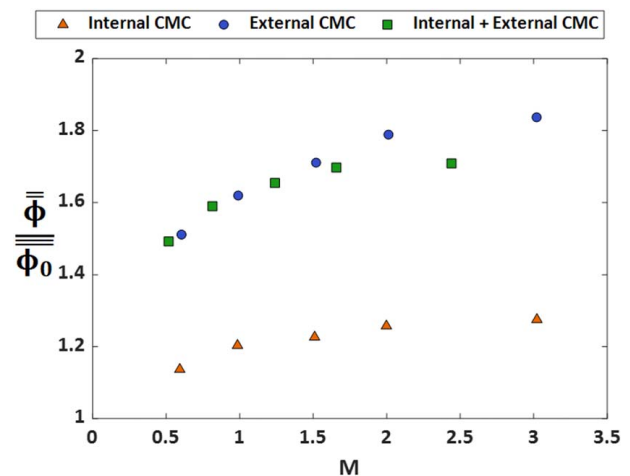
However, for the external weave surface geometries, the addition of the cool fluid layer from film cooling provided a much larger increase in ϕ than for a smooth external surface. For example, ϕ_0 for the external CMC coupon was 40% lower than that of the internal CMC coupon, a significant reduction for the case with no film cooling. However, the decrease between the two coupons was not as significant when comparing the values of ϕ the case with film cooling. In Fig. 10 at $M = 1$, the external CMC coupon saw only a 20% decrease in ϕ when compared to the internal CMC coupon, rather than the 40% decrease seen for ϕ_0. So, when film cooling was introduced to protect the weave surface from the hot external flow, it provided a greater increase in ϕ than the increase seen when film cooling was added to a smooth surface. As such, we see in Fig. 11 that the external CMC and internal + external CMC coupons had significantly increased benefit from the addition of film cooling jets when compared to the internal CMC coupon. These results indicate that film cooling is a key cooling technology for parts containing weave external surfaces, especially when compared to parts with smooth external surfaces.

Conclusion

As CMCs become more prevalent within hot section components of gas turbine engines, it is necessary to understand how their unique weave topology impacts the thermal performance of cooling flows. To further this understanding, test coupons with film cooling holes relevant to true engine scale were additively manufactured. These test coupons contained weave surfaces, representative of CMCs, on the top wall of the internal coolant supply channel, external film cooled surface or both internal and external surfaces. The coupons were tested over a range of blowing ratios to evaluate the effects of the weave geometry on overall effectiveness, with and without film cooling.

Overall effectiveness values without film cooling indicated that the internal CMC coupon with a smooth external surface resulted in significantly increased overall effectiveness levels when compared to the test coupons with an external weave surface. This overall effectiveness increase was because the smooth external surface reduced convective heat transfer between the test coupon and the mainstream flow when compared to an external weave surface.

Flow tests showed that the external CMC coupon, which had a smooth internal surface, saw significantly increased flow parameters at a given pressure ratio compared to the cases with an internal weave surface. The weave surface topology at the inlet of the cooling hole is believed to significantly distort the cooling flow entering the hole. This distortion drove increased pressure loss at the inlet of the film cooling holes, which reduced flow parameter for a given pressure ratio compared to the geometry that was smooth at the inlet of the film cooling holes.

Overall effectiveness results with film cooling showed that increases in blowing ratio caused increases in overall effectiveness for all coupons. Overall effectiveness measurements indicated that the weave surface caused increased mixing between the coolant and mainstream flows compared to a smooth external surface. This increased mixing caused decreased levels of overall effectiveness for coupons with an external weave surface compared to a smooth external surface. The weave surface on the top wall of the internal coolant supply channel increased the heat transfer coefficient of the internal channel and increased in-hole convection when compared to a smooth surface, also increasing levels of overall effectiveness. As such the internal CMC coupon, with a smooth external surface and internal weave surface, saw the highest overall effectiveness.

Overall effectiveness augmentation based on the case with no film cooling indicated that the test coupons with an external weave surface had the same augmentation, while the internal CMC coupon, which had a smooth external surface, saw lower augmentation levels compared to the other two geometries. The lower augmentation levels for the smooth external surface were driven by the lesser benefit of film cooling to the cooling of the coupon, compared to the coupons with an external weave surface.

This study provided valuable knowledge for turbine designers who wish to implement film cooling into components made of CMC. The results prominently indicated the importance of considering the weave surface topology of the CMC when implementing this new material.

Acknowledgment

Conflict of Interest

There are no conflicts of interest.

Data Availability Statement

The datasets generated and supporting the findings of this article are obtainable from the corresponding author upon reasonable request.

Nomenclature

h = convective heat transfer coefficient
$\dot{m}$ = mass flowrate
t = coupon wall thickness
D = film cooling hole diameter
H = mainstream channel height
L = test coupon length
M = blowing ratio, $(\dot{m}_f/A_{\min})/(\rho_\infty U_\infty)$
P = pressure
R = gas constant
S = lateral distance between holes, pitch
T = temperature
U = maximum/centerline velocity
V = mass average velocity
W = test coupon width
X = streamwise distance
c_p = specific heat capacity
A_c = cross-sectional flow area
$A_{\min}$ = minimum cross-sectional area of cooling hole meter
D_h = hydraulic diameter, $4A_c/p$
K_s = sandgrain roughness
S_a = arithmetic mean roughness
Bi = Biot number, $h_\infty t/\kappa$
DR = density ratio, ρ_c/ρ_∞
FP = mass flow parameter, $\dot{m}(RT_c)^{0.5}/P_c A_c$
Ma = Mach number
Nu = Nusselt number, hD_h/k_{air}
PR = pressure ratio
Pr = Prandtl number
Re_{Dh} = Reynolds number, $V_i D_h/\nu$
Re_L = Reynolds number, $V_\infty L/\nu$

Greek Symbols

θ = normalized temperature, $T - T_{\text{in}}/T_s - T_{\text{in}}$
κ_{air} = thermal conductivity of air
ν = kinematic viscosity
ρ = fluid density
ϕ = overall effectiveness, $(T_\infty - T_s)/(T_\infty - T_c)$
$\overline{\phi}$ = laterally averaged overall effectiveness

$\bar{\phi}$ = area averaged overall effectiveness

$\bar{\bar{\phi}}_0$ = overall effectiveness without film cooling

Subscripts

c = coolant
CMC = weave surface
cl = centerline of film hole
e = external mainstream channel
f = weave fabric
h = region upstream and adjacent of film hole breakout
i = coupon internal channel
in = channel inlet
s = coupon surface
smooth = smooth surface
t = weave tow
w = weave peak
∞ = mainstream

References

[1] Zhu, D., 2018, "Aerospace Ceramic Materials: Thermal, Environmental Barrier Coatings and SiC/SiC Ceramic Matrix Composites for Turbine Engine Applications," NASA/TM—2018-219884.
[2] Yin, X. W., Cheng, L. F., Zhang, L. T., Travitzky, N., and Greil, P., 2017, "Fibre-Reinforced Multifunctional SiC Matrix Composite Materials," Int. Mater. Rev., **62**(3), pp. 117–172.
[3] Walock, M. J., Heng, V., Nieto, A., Ghoshal, A., Murugan, M., and Driemeyer, D., 2018, "Ceramic Matrix Composite Materials for Engine Exhaust Systems on Next-Generation Vertical Lift Vehicles," ASME J. Eng. Gas Turbines Power, **140**(10), p. 102101.
[4] Watanabe, F., Nakamura, T., and Shinohara, K. I., 2016, "The Application of Ceramic Matrix Composite to Low Pressure Turbine Blade," GT2016-56614.
[5] Watanabe, F., Nakamura, T., and Mizokami, Y., 2017, "Design and Testing for Ceramic Matrix Composite Turbine Vane," GT2017-63264.
[6] Ohnabe, H., Masaki, S., Onozuka, M., Miyahara, K., and Sasa, T., 1999, "Potential Application of Ceramic Matrix Composites to Aero-Engine Components," Compos. Part A Appl. Sci. Manuf., **30**(4), pp. 489–496.
[7] Schulz, A., and Behrendt, T., 2016, "Effusion Cooled Combustor Liner Tiles With Modern Cooling," GT2016-56598.
[8] Presby, M. J., Nesredin, K., Sanchez, L. J., Faucett, D. C., Choi, S. R., and Morscher, G. N., 2019, "Life-Limiting Behavior of an Oxide/Oxide Ceramic Matrix Composite at Elevated Temperature Subject to Foreign Object Damage," ASME J. Eng. Gas Turbines Power, **141**(3), p. 031012.
[9] Krishna, K., and Ricklick, M., 2017, "Heat Transfer Analysis of Jet Impingement Cooling on a Simulated Ceramic Matrix Composite Surface," GT2017-64991.
[10] Wilkins, P. H., Lynch, S. P., Thole, K. A., Quach, S., and Vincent, T., 2021, "Experimental Heat Transfer and Boundary Layer Measurements on a Ceramic Matrix Composite Surface," ASME J. Turbomach., **143**(6), p. 061010.
[11] Nemeth, N. N., Mital, S. K., and Lang, J., 2010, "Evaluation of Solid Modeling Software for Finite Element Analysis of Woven Ceramic Matrix Composites," NASA/TM 2010-216250.
[12] Wilkins, P. H., Lynch, S. P., Thole, K. A., Quach, S., Vincent, T., and Mongillo, D., 2021, "Effect of a Ceramic Matrix Composite Surface on Film Cooling," GT2021-59602.
[13] Cory, T. M., Edelson, R. D., Thole, K. A., Quach, S., Vincent, T., and Mongillo, D., 2021, "Impact of Ceramic Matrix Composite Topology on Friction Factor and Heat Transfer," GT2021-59588.
[14] Lin, H., Brown, L. P., and Long, A. C., 2011, "Modelling and Simulating Textile Structures Using TexGen," Adv. Mater. Res., **331**(1), pp. 44–47.
[15] Schroeder, R. P., and Thole, K. A., 2014, "Adiabatic Effectiveness Measurements for a Baseline Shaped Film Cooling Hole," GT2014-25992.
[16] Stimpson, C. K., Snyder, J. C., Thole, K. A., and Mongillo, D., 2017, "Scaling Roughness Effects on Pressure Loss and Heat Transfer of Additively Manufactured Channels," ASME J. Turbomach., **139**(2), p. 021003.
[17] Stimpson, C. K., Snyder, J. C., Thole, K. A., and Mongillo, D., 2018, "Effectiveness Measurements of Additively Manufactured Film Cooling Holes," ASME J. Turbomach., **140**(1), p. 011009.
[18] Stimpson, C. K., Snyder, J. C., Thole, K. A., and Mongillo, D., 2018, "Effects of Coolant Feed Direction on Additively Manufactured Film Cooling Holes," ASME J. Turbomach., **140**(11), p. 111001.
[19] Kays, W. M., Crawford, M. E., and Weigand, B., 2005, Convective Heat and Mass Transfer, McGraw-Hill, Boston, MA.
[20] Figliola, R. S., and Beasley, D. E., 1995, "Theory and Design for Mechanical Measurements, Second Edition," Eur. J. Eng. Educ., **20**(3), pp. 386–387.
[21] Hay, N., Lampard, D., and Khaldi, A., 1994, "The Coefficient of Discharge of 30 Deg Inclined Film Cooling Holes With Rounded Entries or Exits," 94-GT-180.